Supporting information

Engineering a Local Potassium Cation Concentrated Microenvironment toward Ampere-Level Current Density Hydrogen Evolution Reaction

Lei Gao,‡[a] Feixiang Bao,‡[a] Xin Tan,*[b] Mengfan Li,[a] Zhen Shen,[c] Xuli Chen,[a] Ziyi Tang,[a] Wenchuan Lai,[a] Yangfan Lu,[d] Peifeng Huang,[a] Chao Ma,[a] Sean C. Smith,[e] Zhizhen Ye,[d] Zheng Hu*[c] and Hongwen Huang*[af]

[a] *College of Materials Science and Engineering, State Key Laboratory of Advanced Design and Manufacturing for Vehicle Body, Hunan University, Changsha, Hunan 410082, P. R. China. Email: huanghw@hnu.edu.cn*

[b] *Institute for Carbon Neutralization, College of Chemistry and Materials Engineering, Wenzhou University, Wenzhou, Zhejiang 325035, P.R. China. Email: xintan@wzu.edu.cn*

[c] *Key Laboratory of Mesoscopic Chemistry of MOE and Jiangsu Provincial Lab for Nanotechnology, School of Chemistry and Chemical Engineering, Nanjing University, Nanjing, Jiangsu 210023, P. R. China. Email: zhenghu@nju.edu.cn*

[d] *State Key Laboratory of Silicon Materials, School of Materials Science and Engineering, Zhejiang University, Hangzhou 310027, P. R. China.*

[e] *Integrated Materials Design Laboratory, Department of Materials Physics, Research School of Physics, The Australian National University, Canberra, ACT 2601, Australia.*

[f] *Shenzhen Research Institute of Hunan University, Shenzhen, Guangdong 518055, P. R. China.*

† Electronic supplementary information (ESI) available: Experimental section, TEM and STEM images, XPS and XRD spectrum, TEM-EDS spectrum, CV and LSV curves, CO stripping voltammogram, Nyquist plots, theoretical model structures, and Tables.

‡ These authors contributed equally to this work.

Methods

Chemicals. Ruthenium(III) acetylacetonate ($Ru(acac)_3$, 97%) was purchased from Shanghai Aladdin Biochemical Technology Co. Ltd. Nickel(II) acetylacetonate ($Ni(acac)_2$, 98%) was purchased from Adamas. Polyvinylpyrrolidone (PVP, MW ≈ 55000) and Nafion (5 wt%) were purchased from Sigma-Aldric. Benzyl alcohol ($C_6H_5CH_2OH$, analytical reagent, ≥ 99%), resorcinol ($C_6H_6O_2$, analytical reagent, ≥ 99.5%), ethanol (CH_3CH_2OH, analytical reagent, ≥ 99.7%), isopropanol (C_3H_8O, analytical reagent, ≥ 99.7%) were purchased from Sinopharm Chemical Reagent Co. Ltd. (Shanghai, China). The DI-water (18.2 MΩ cm^{-1}) was freshly prepared through an ultra-pure purification system (Master-515Q, HHitech). All the chemicals were used without further purification.

Synthesis of NA-Ru_3Ni. Typically, $Ru(acac)_3$ (7.5 mg, 0.0188 mmol), $Ni(acac)_2$ (1.6 mg, 0.0063 mmol), 50 mg PVP, 50 mg resorcinol and 5 mL benzyl alcohol were added into a vial (volume: 30 mL). The mixture was ultrasonicated for around 30 minutes to obtain a homogeneous solution, and then the solution was proceeded at 180 °C for 1 hours in an oil bath. After the resulting solution was cooled to room temperature, products were collected by centrifugation, and washed three times with ethanol.

Synthesis of Ru_3Ni-300 and Ru_3Ni-600 samples. The obtained NA-Ru_3Ni was loaded onto Vulcan XC-72 carbon to obtain a NA-Ru_3Ni/C (33.3 wt% metal loading). For contrast, the NA-Ru_3Ni/C was annealed under 300 ℃ for 5 h at the heating rate of 10 °C min^{-1} under a reduction atmosphere (5% H_2, 95% N_2) in a tube furnace and then cooled naturally to room temperature. The annealed product was washed several times with DI water and ethanol, resulting in the final Ru_3Ni-300 sample. The Ru_3Ni-600 sample was obtained using the same procedure except that the reaction condition was changed to 600 °C for 2 h.

Characterizations. The crystalline phases of all samples were evaluated by X-ray diffraction (XRD, Rigaku Miniflex-600) with a Cu Kα radiation (λ= 0.15 nm, 40 kV). TEM images were

obtained using a JEM-2100plus electron microscope. HAADF-STEM images and elemental mapping results were recorded on a Themis Z (3.2) with spherical aberration corrector operating at 300 kV. Elemental analysis of Ru and Ni were quantitatively conducted by ICP-MS with a SPECTRO BLUE SOP. The chemical states of Ru and Ni were investigated by XPS using an Escalab 250Xi equipped with an Al Ka (1486.6 eV) excitation source. The binding energies in the XPS spectral were calibrated by referencing C 1s to 284.8 eV.

Electrochemical measurements in three-electrode system. All the electrochemical tests were conducted in a three-electrode system using a DH7001A electrochemical workstation (Donghua Analytical Instrument, China). In the electrochemical measurements, the Hg/HgO reference electrode was carefully calibrated with respect to the RHE by testing cyclic voltammogram in a highly-pure H_2-saturated 1 M KOH with Pt wires used as working electrode and counter electrode. Therefore, the potential with respect to RHE in our measurements can be calculated as follows:

$$E(\text{RHE}) = E(\text{Hg/HgO}) + 0.935\ \text{V}.$$

Prior to the electrochemical measurements, the carbon-support catalysts were prepared. Typically, 1 mg NA-Ru_3Ni was uniformly dispersed in an ethanol solution (2 mL) with ultrasonicating. Then this solution was dropwise added to an ethanol solution containing 2 mg carbon support (Vulcan XC-72) and ultrasonicating for 30 min. The carbon-supported catalyst was collected by centrifugation and dried in a vacuum oven. Subsequently, the carbon-supported catalyst was treated in an oven at 250 ^{o}C for 1 h and termed as NA-Ru_3Ni/C. Finally, the NA-Ru_3Ni/C catalyst was uniformly dispersed in the mixed solution of 310 μL isopropanol, 930 μL ethanol and 10 μL Nafion solution (5 wt%), and then 20 μL of the NA-Ru_3Ni/C catalyst ink was dropped on the surface of the glassy carbon electrode and dried at room temperature.

All the electrochemical tests were carried out in 1 M KOH solution. Linear sweep voltammetry was performed at 5 mV s^{-1} and all the polarization curves were *iR*-corrected unless otherwise stated. The current density was obtained by normalizing the current to the geometric surface of the work electrode. EIS was performed with 5 mV amplitude in a frequency range from 0.1 to 1000000

Hz at the open circuit voltage to obtain the solution resistance (Figure S37). The ECSAs of catalysts were calculated by integrating the CO adsorption area from the CO-stripping curves, and the charge density for the monolayer adsorption of CO was assumed as 420 μC cm^{-2}. For CO stripping measurements, CO gas (99.99%) was fed into the electrolyte with holding a potential of 0.1 V_{RHE} for 30 min. Then, N_2 gas was purged to remove CO from the electrolyte, and the CO stripping curves were recorded between 0.1 V_{RHE} and 1.0 V_{RHE} with a sweep rate of 50 mV s^{-1}. The accelerated durability tests were performed at room temperature in N_2-saturated 1.0 M KOH aqueous solution by applying the cyclic potential sweeps between 0.1 V_{RHE} and -0.1 V_{RHE} at scan rate of 100 mV s^{-1} for 10k cycles. The TOF (H^2 s^{-1}) values of catalysts were calculated based on the number of active sites using the following equation:

$$\mathrm{TOF} = I / (2Fn)$$

where I (A) is the current during the LSV measurement at a specific overpotential, F is Faraday constant (96485.3 C mol^{-1}), and n is the number of active sites (mol). The number 2 means 2 electrons to generate one H_2 molecule.

Electric-field-induced K^+ accumulation measurements. Electric-field-induced K^+ accumulation was measured in 1 M KOH. NA-Ru_3Ni/C, Ru_3Ni-300/C and Ru_3Ni-600/C catalysts were tested with constant potential of -0.1 V_{RHE}. When the testing time reached 120 s, the electrode was directly raised above the electrolyte. After removing the applied potential, the electrodes were immersed in 20 mL pure water, and adsorbed K^+ of catalysts surface was released into the pure water. Then, we used the ICP-MS to check the amount of K^+, which were normalized by using ECSA.

AEM electrolysis. The ink of NA-Ru_3Ni/C catalyst was air brushed onto the gas diffusion layer (GDL, YLS30T) with a loading about 0.048 mg cm^{-2} to form cathode electrode (0.5 cm^2). The anode electrode was prepared by brushing NA-Ru_3Ni/C inks on 300 μm Nickel foam, which was degreased and pretreated in 0.1 M HCl solution before using to remove the passive oxide layer and other contaminants. Subsequently, an anion exchange membrane (Sustainion X37-50) was

sandwiched between the cathode and anode catalyst to construct the electrolyser (NA-Ru_3Ni/C||NA-Ru_3Ni/C), and the 1 M KOH was fed to both sides of the electrolyser.

COMSOL Multiphysics simulations. In this work, we performed the COMSOL Multiphysics finite-element-based solver to simulate the electric field and K^+ density on the surface of the electrodes. Electric field E was computed as the opposite gradient of the electric potential V as follows: $\boldsymbol{E} = -\nabla V$. The electric conductivity of the electrode (ruthenium) was taken to be 1.37×10^7 S m^{-1}. The conductivity of 1 M KOH solution was assumed to be 2.0 S m^{-1}.[1] Therefore, we computed the charge density ρ using Gauss's law for electric field: $\rho = \varepsilon_r\varepsilon_0\nabla\cdot E$, where ε_0 denoted the dielectric function for a vacuum, and ε_r denoted the dielectric function of the materials, and equals 80 for the electrolyte and 1 for ruthenium. The 'Electrostatics' and the 'Transport of diluted species' modules were combined to solve the potassium ion density in the electrical double layer. The Poisson-Nerst-Planck equations were solved in the steady state:

$$\nabla\cdot\left(D\nabla c_i + \frac{Dz_i e}{k_B T}c_i\nabla V\right) = 0$$

Here c_i with $i \in \{K^+, OH^-\}$ are the concentrations of the potassium or hydroxyl ion, z_i is the valency of ions, e is the elementary charge, k_B is Boltzmann constant, the absolute temperature T was taken is 297.3 K. The diffusion coefficients D of the potassium ion, the hydroxyl ion, and the proton in water were taken to be 2.14×10^{-9} m^2 s^{-1}, 2.71×10^{-9} m^2 s^{-1} and 7.10×10^{-9} m^2 s^{-1}.[2,3] Two-dimensional axisymmetric models were built to represent the three-dimensional NA-Ru_3Ni, Ru_3Ni-300 and Ru_3Ni-600 structures used in this work. Triangular meshes were used for all simulations.

DFT calculations. All of the spin-polarized DFT calculations were performed using the VASP program,[4-6] which uses a plane-wave basis set and a projector augmented wave method (PAW) for the treatment of core electrons.[4] The Perdew, Burke, and Ernzerhof exchange-correlation functional within a generalized gradient approximation (GGA-PBE)[7] was used in our calculations, and the van der Waals (vdW) correction proposed by Grimme (DFT-D3)[8] was employed due to its

good description of long-range vdW interactions. For the expansion of wavefunctions over the plane-wave basis set, a converged cutoff was set to 450 eV.

The structural models of $Ru_3Ni(0001)$ surface were constructed of four atomic layers with the bottom two layers fixed in their respective bulk positions and all the other atoms fully relaxed. Here we included a water bi-layer to describe explicitly the polarization involved in proton transfer. The positions of these water molecules were optimized with VASPsol. The K cation in electrolyte is modelled by initially inserting a K atom at 3.0 Å away from the $Ru_3Ni(0001)$ surface. As expected, the K atom is spontaneously oxidized to K^+ in liquid water, and one electron will simultaneously emerge on the $Ru_3Ni(0001)$ surface. The vacuum space was set to larger than 18 Å in the *z* direction to avoid interactions between periodic images. In geometry optimizations, all the atomic coordinates were fully relaxed up to the residual atomic forces smaller than 0.01 eV $Å^{-1}$, and the total energy was converged to 10^{-5} eV. The Brillouin zone integration was performed on the (5 × 5 × 1) Monkhorst–Pack k-point mesh.[9] The activation energy barriers of water dissociation reaction were calculated through the climbing image nudged elastic band (NEB) method,[10] in which all of force components perpendicular to the tangent of the reaction path were relaxed to be less than 0.05 eV $Å^{-1}$.

For alkaline HER, the overall HER mechanism includes the water dissociation reaction to supply hydrogen and the adsorption/combination of reaction H*.[11] The ΔG_{H^*} is proven to be a key descriptor to characterize the HER activity of the electrocatalyst from the thermodynamic viewpoint. The optimum value of $|\Delta G_{H^*}|$ should be zero. The ΔG_{H^*} is calculated as follows:[12]

$$\Delta G_{H^*} = \Delta E_{H^*} + \Delta E_{ZPE} - T\Delta S_H$$

where ΔE_{H^*} is the binding energy of adsorbed hydrogen, and ΔE_{ZPE} and ΔS_H are the difference in zero point energy (ZEP) and entropy between the adsorbed hydrogen and hydrogen in the gas phase, respectively. As the contribution from the vibrational entropy of hydrogen in the adsorbed state is negligibly small, the entropy of hydrogen adsorption is $\Delta S_H \approx -\frac{1}{2} S_{H_2}$, where S_{H_2} is the

entropy of H_2 in the gas phase at the standard conditions. Therefore, the ΔG_{H^*} value for $Ru_3Ni(0001)$ surface should be $\Delta E_H + 0.24$ eV.[12]

To evaluate the local electric field located between the negatively charged metal surface and electrolyte solution, we used the parallel plate capacitor model consists of two unevenly charged plates ($Q1$ and $Q2$) with an area of S. We defined the local electric field as $E = \frac{(Q1 + Q2)/S}{2\varepsilon}$, where ε represents the absolute permittivity of water.

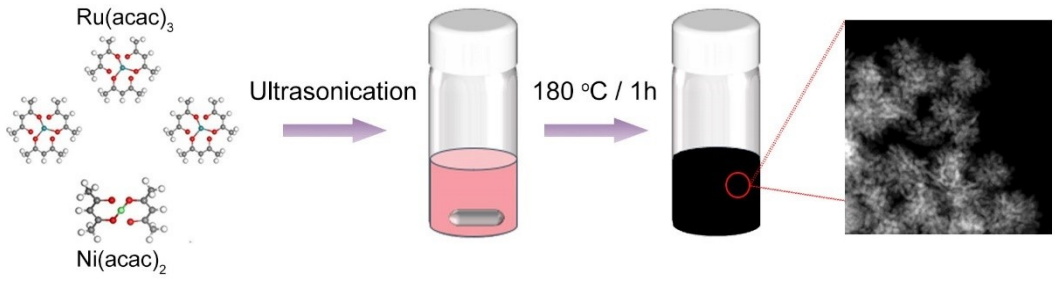

Figure S1. Schematic illustration showing the co-reduction synthesis of NA-Ru_3Ni.

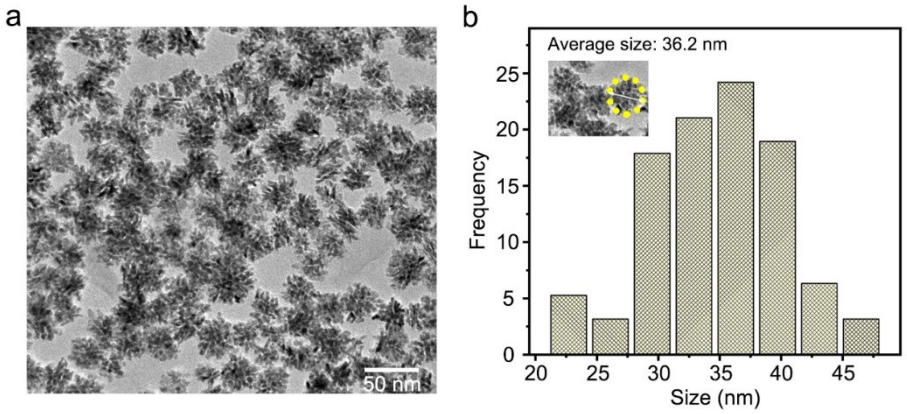

Figure S2. (a) TEM image and (b) histogram for size distribution of NA-Ru_3Ni.

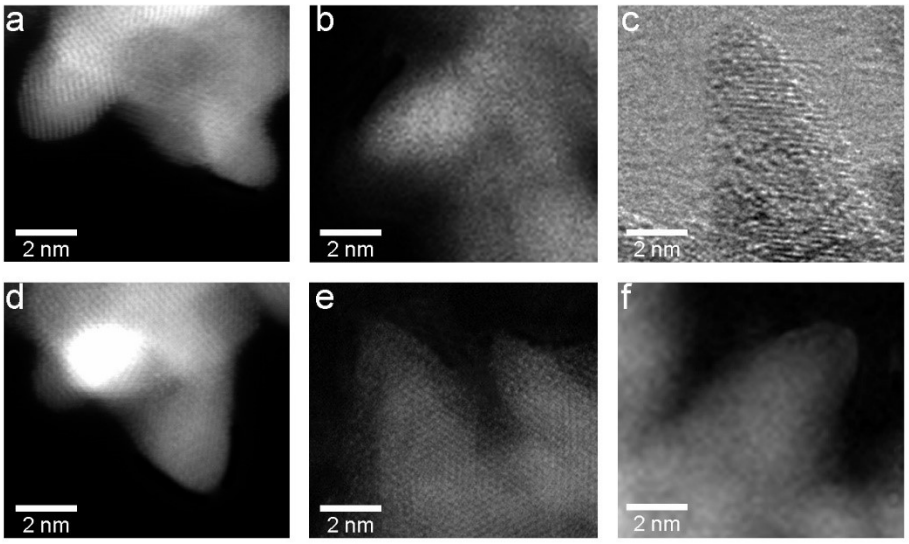

Figure S3. (a-f) HRTEM images of nano cones from different positions.

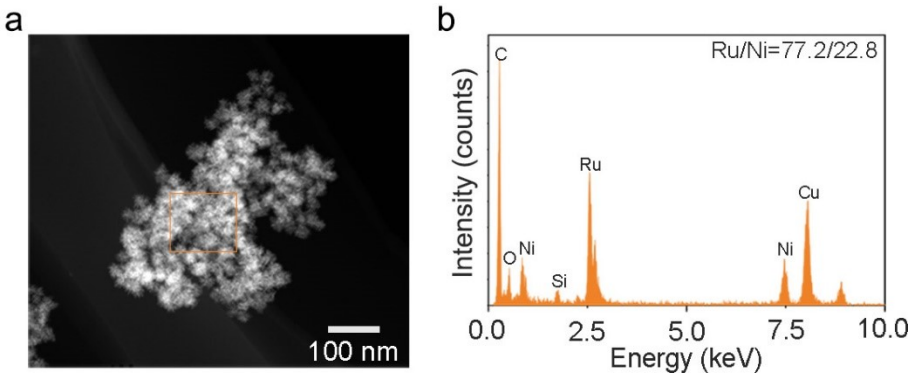

Figure S4. (a) HAADF-STEM image and (b) STEM-EDS spectrum of NA-Ru_3Ni.

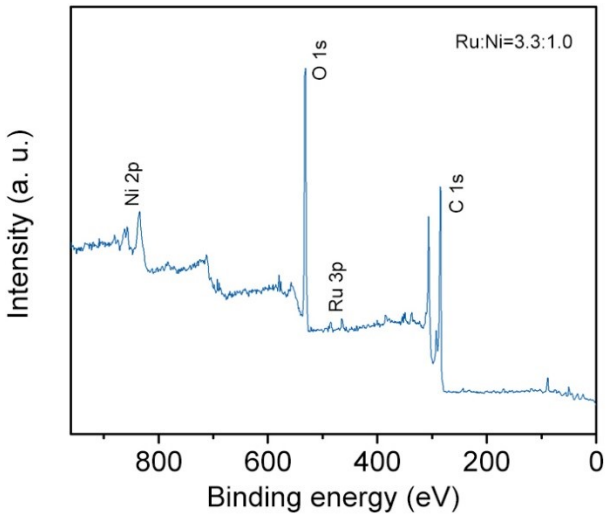

Figure S5. The XPS survey spectrum of the NA-Ru_3Ni.

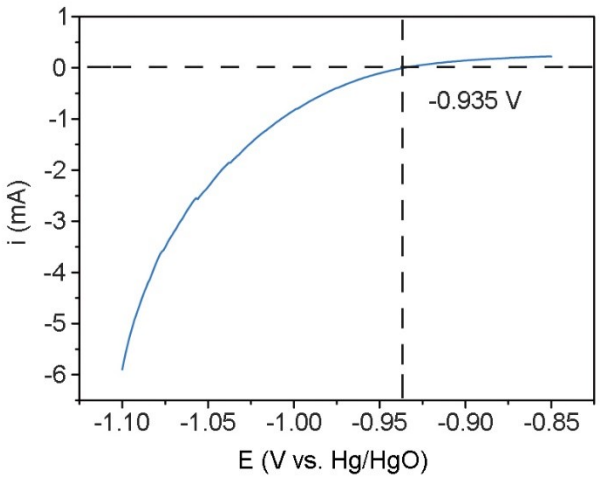

Figure S6. Potential calibration for the Hg/HgO reference electrode in 1 M KOH solution.

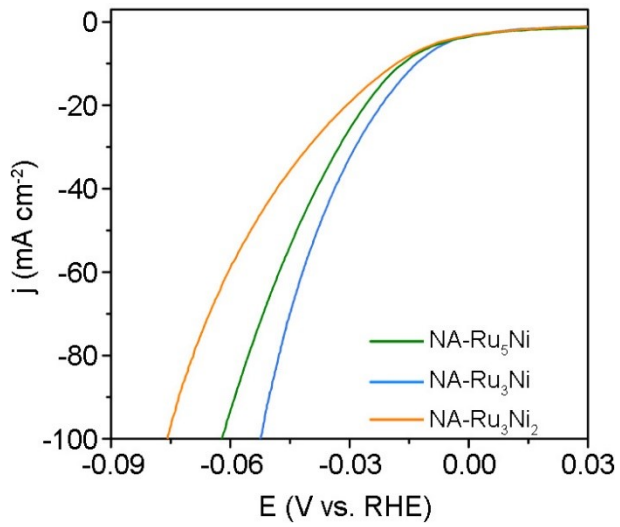

Figure S7. Polarization curves (with iR-correction) of different catalysts recorded in 1 M KOH solutions at a sweep rate of 5 mV s^{-1}.

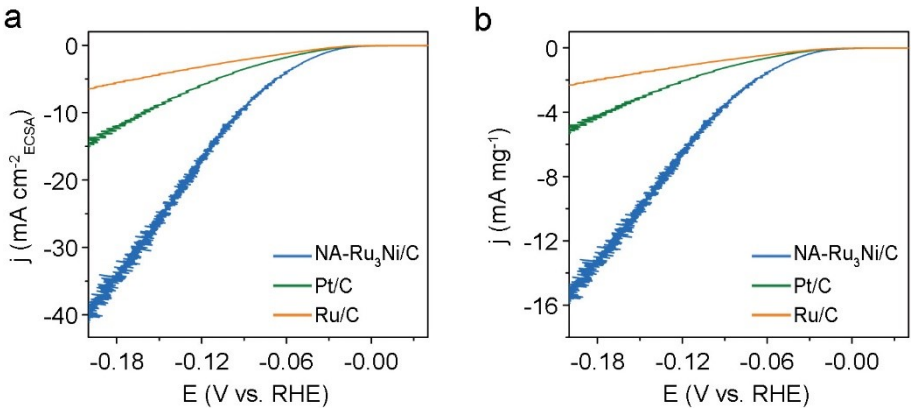

Figure S8. (a) The specific activities and (b) mass activities of different catalysts.

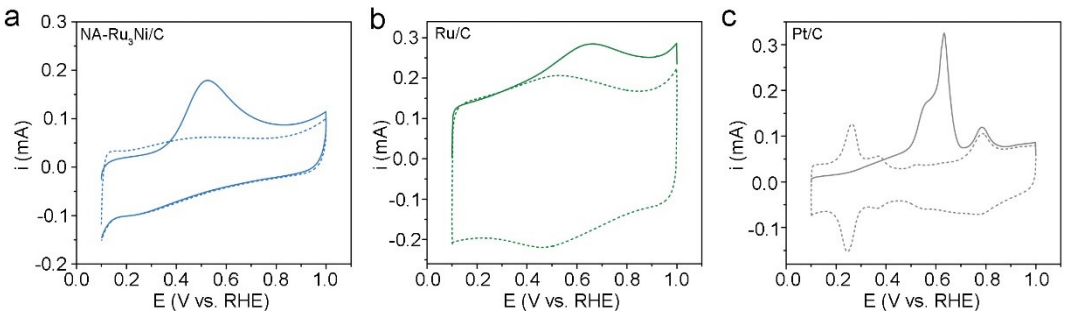

Figure S9. Cyclic voltammograms (CVs) in N_2-saturated electrolyte (dotted lines) and CO stripping curves (solid lines) to estimate the ECSAs for (a) NA-Ru_3Ni/C, (b) Ru/C, and (c) Pt/C catalysts.

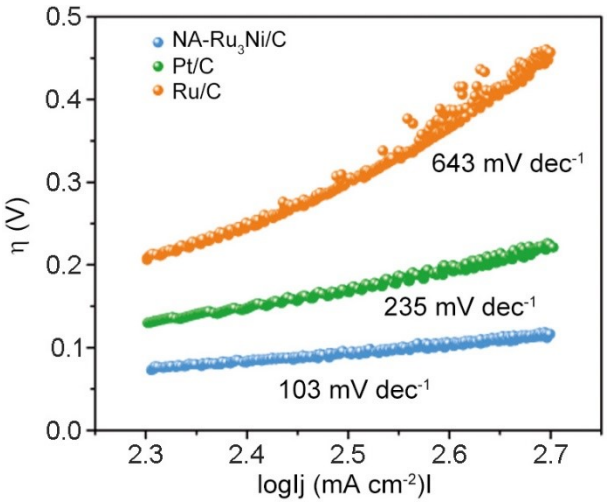

Figure S10. Tafel plots of NA-Ru_3Ni/C, Pt/C, and Ru/C catalysts at the current density of 300-500 mA cm^{-2}.

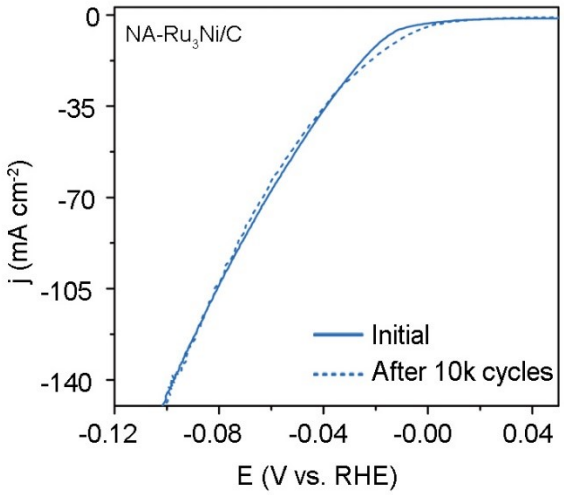

Figure S11. HER polarization curves of NA-Ru_3Ni/C before and after 10k cycles.

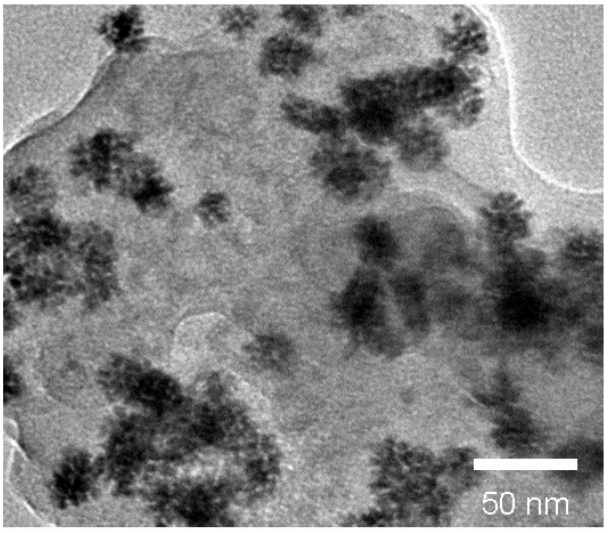

Figure S12. TEM image of NA-Ru_3Ni/C catalyst after the long-term testing of 1800 h.

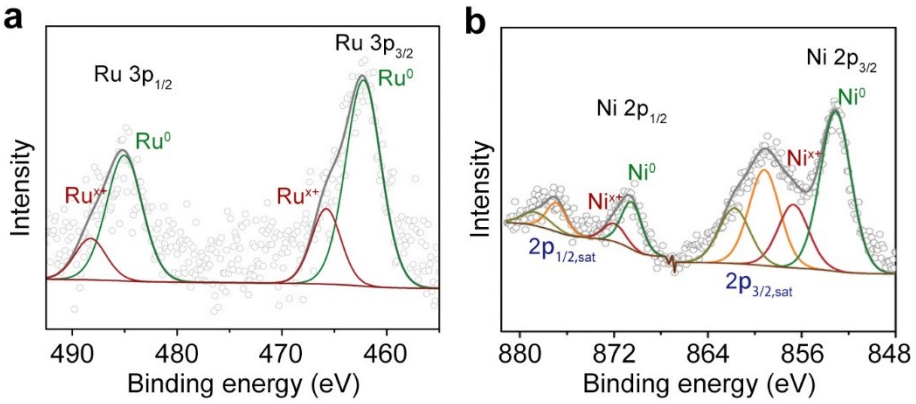

Figure S13. High-resolution XPS spectra of (a) Ru 3p and (b) Ni 2p for NA-Ru_3Ni/C catalyst after the long-term testing of 1800 h.

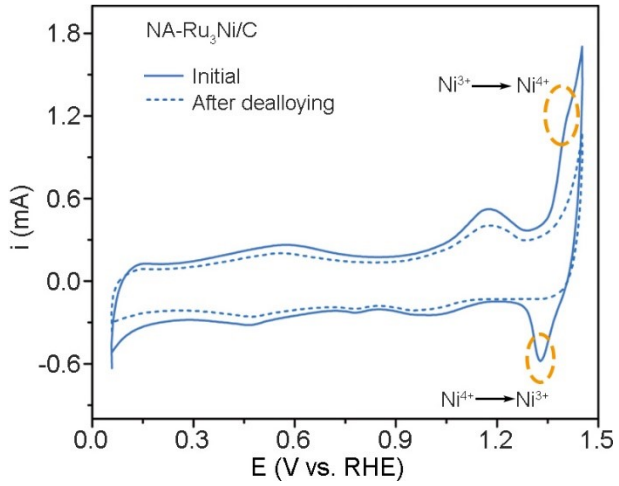

Figure S14. CV curves of NA-Ru_3Ni/C catalyst before and after dealloying.

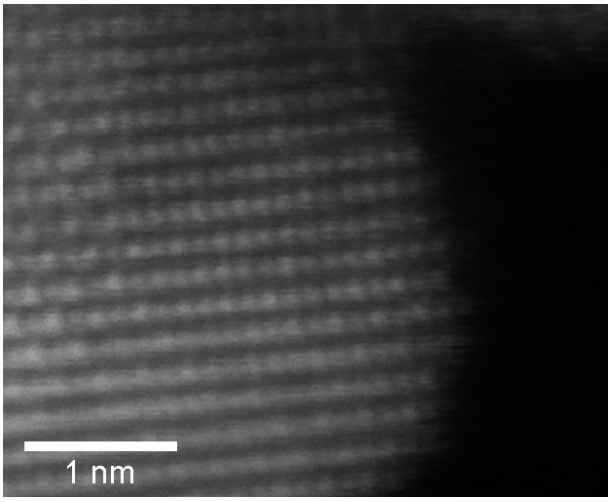

Figure S15. HAADF-STEM of NA-Ru_3Ni with removing surface Ni atoms.

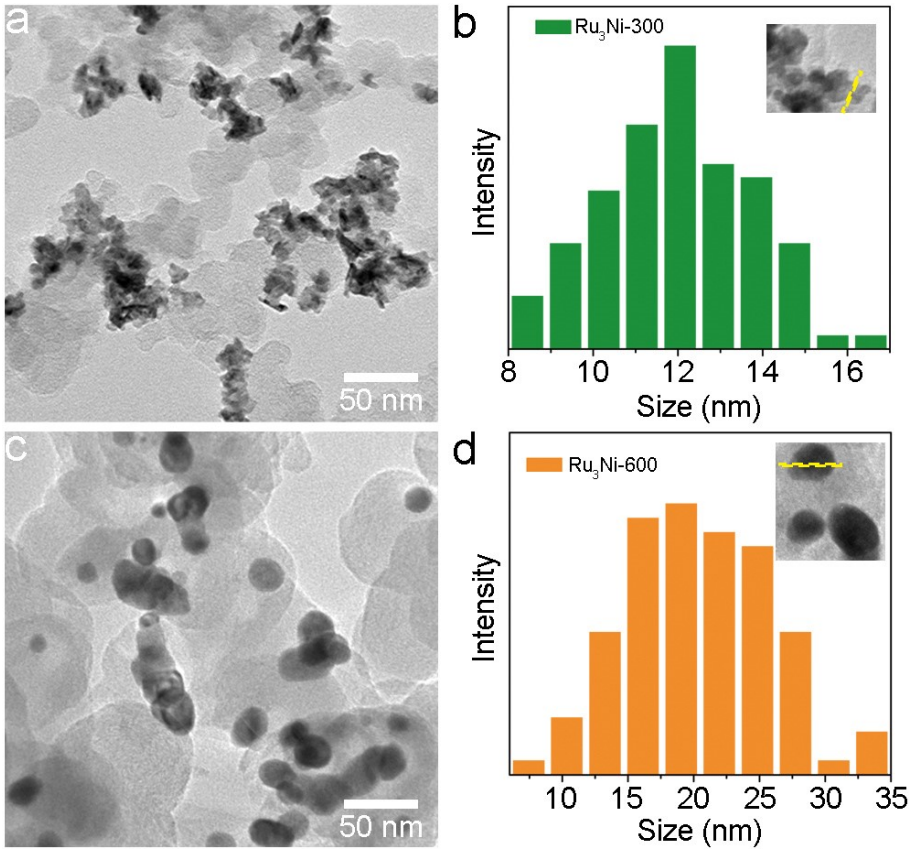

Figure S16. (a) TEM image and (b) histogram of diameter for Ru_3Ni-300. (c) TEM image and (d) histogram of diameter for Ru_3Ni-600.

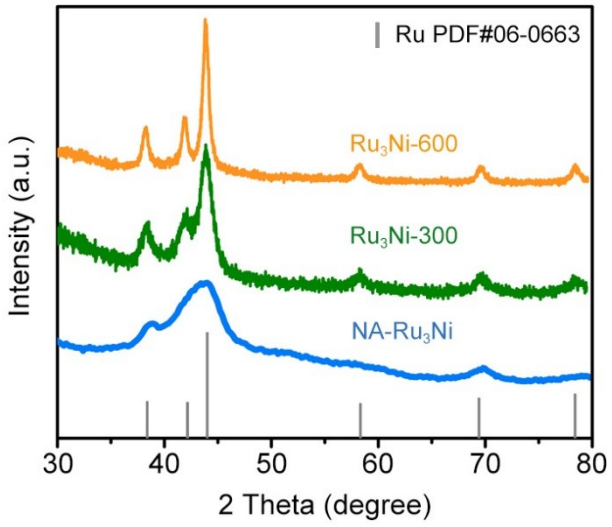

Figure S17. XRD patterns of NA-Ru_3Ni, Ru_3Ni-300, Ru_3Ni-600 samples.

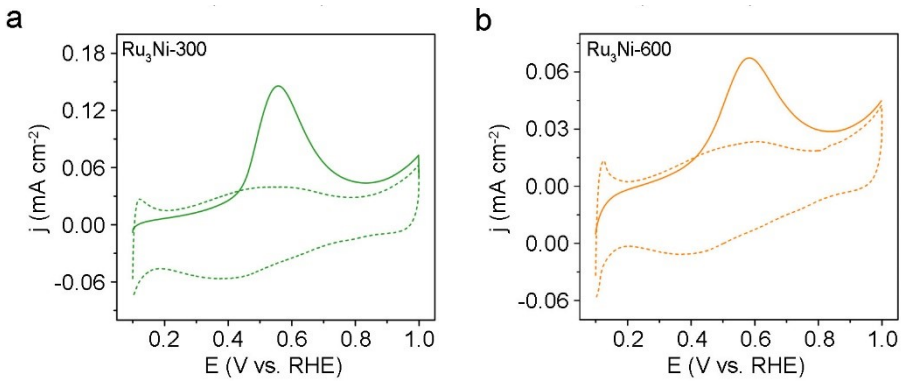

Figure S18. CVs in N_2-saturated electrolyte (dotted lines) and CO stripping curves (solid lines) to estimate the ECSAs for (a) Ru_3Ni-300/C and (b) Ru_3Ni-600/C catalysts.

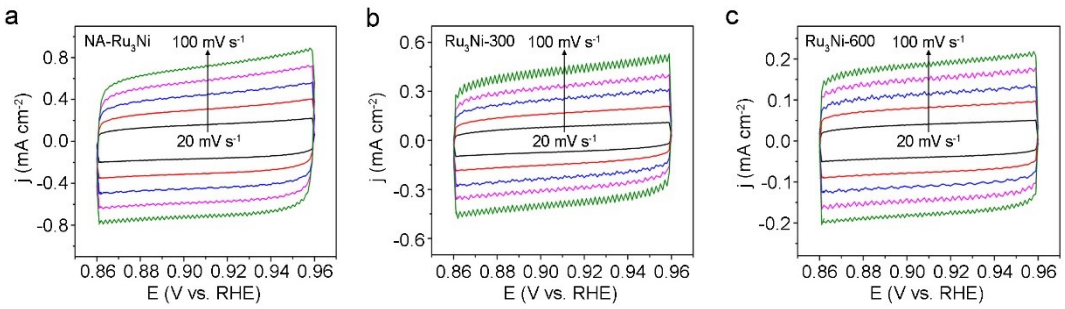

Figure S19. CVs at different scan rates of (a) NA-Ru_3Ni/C, (b) Ru_3Ni-300/C, and (c) Ru_3Ni-600/C.

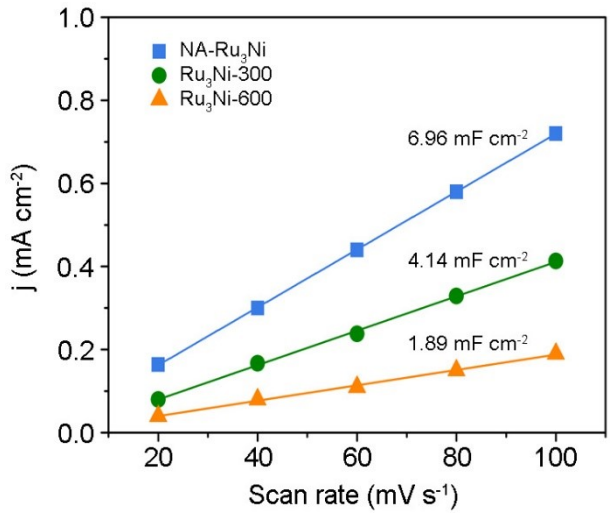

Figure S20. Double-layer capacitance (C_{dl}) of NA-Ru_3Ni/C, Ru_3Ni-300/C, and Ru_3Ni-600/C catalysts obtained from CVs at different scan rates.

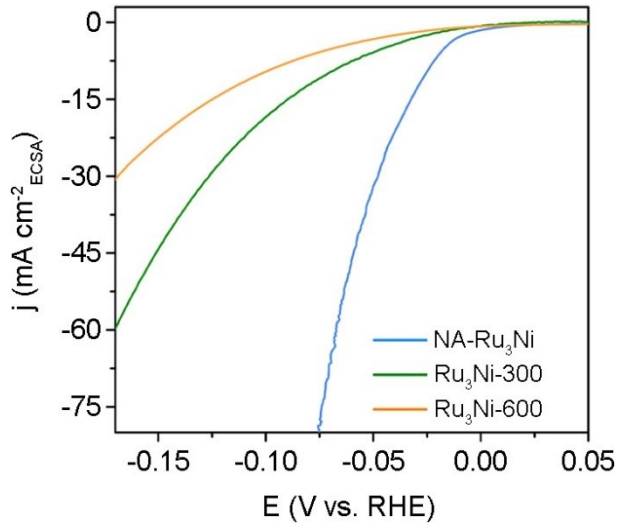

Figure S21. The polarization curves of different catalysts normalized to the ECSA.

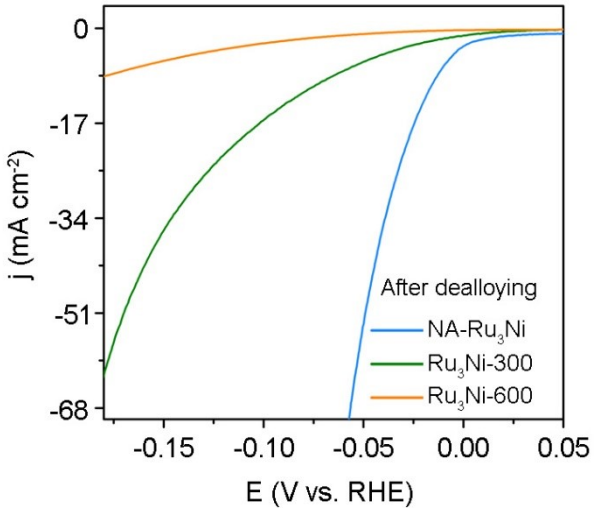

Figure S22. The polarization curves of different catalysts normalized to the geometry area after dealloying.

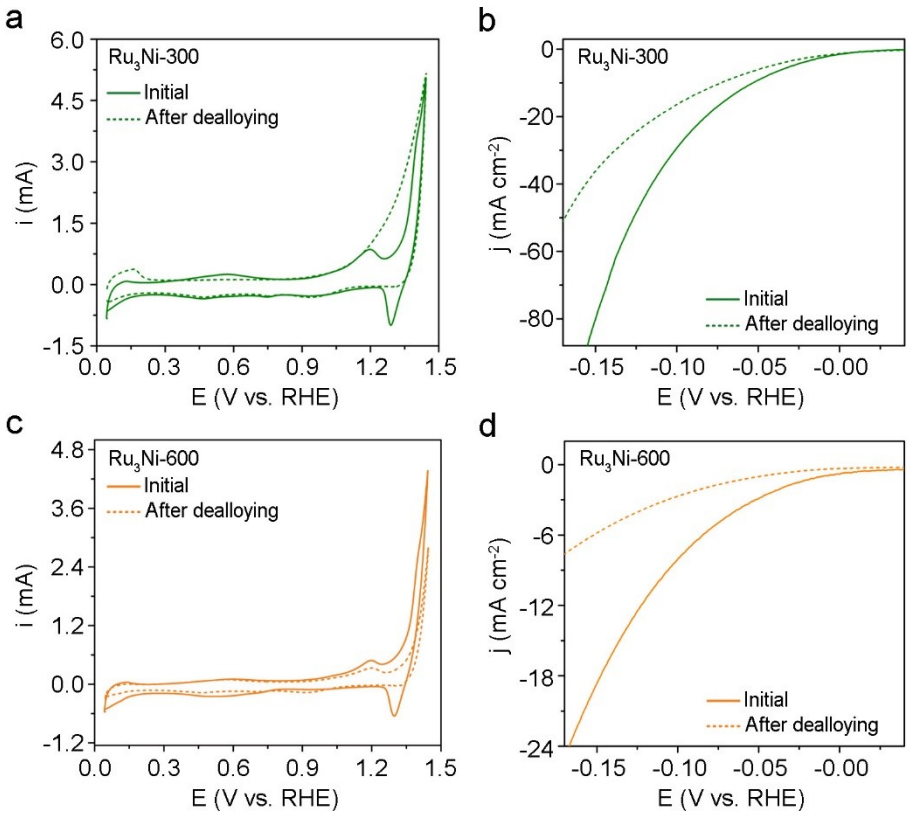

Figure S23. CV (a) and HER polarization (b) curves of Ru_3Ni-300 before and after dealloying. CV (c) and HER polarization (d) curves of Ru_3Ni-600 before and after dealloying.

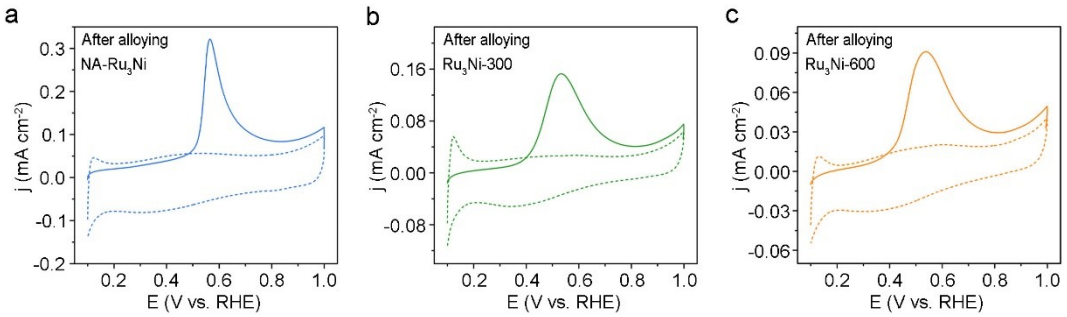

Figure S24. CVs in N_2-saturated electrolyte (dotted lines) and CO stripping curves (solid lines) to estimate the ECSAs for (a) NA-Ru_3Ni/C, (b) Ru_3Ni-300/C, and (c) Ru_3Ni-600/C catalysts after dealloying.

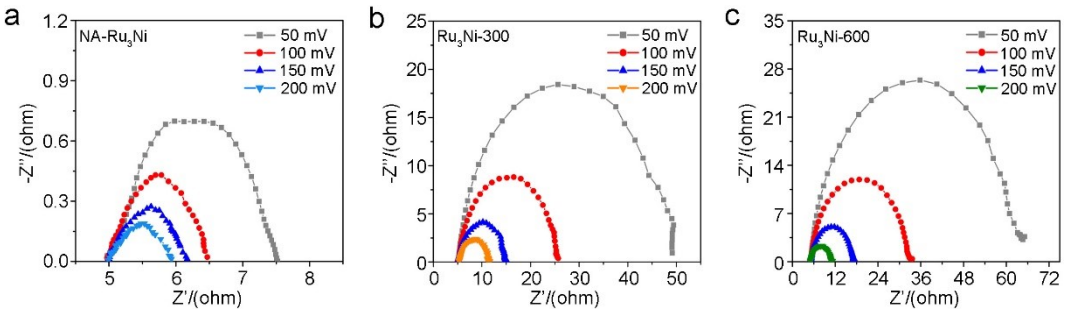

Figure S25. The Nyquist plots of (a) NA-Ru_3Ni/C, (b) Ru_3Ni-300/C, and (c) Ru_3Ni-600/C at different overpotential.

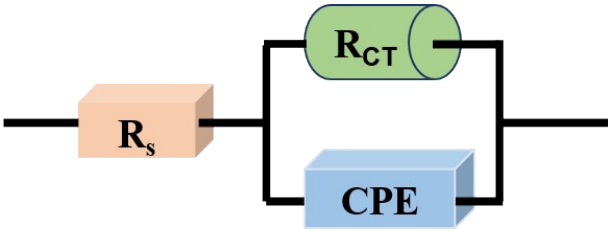

Figure S26. Equivalent circuit of the electrochemical impedance spectrum.

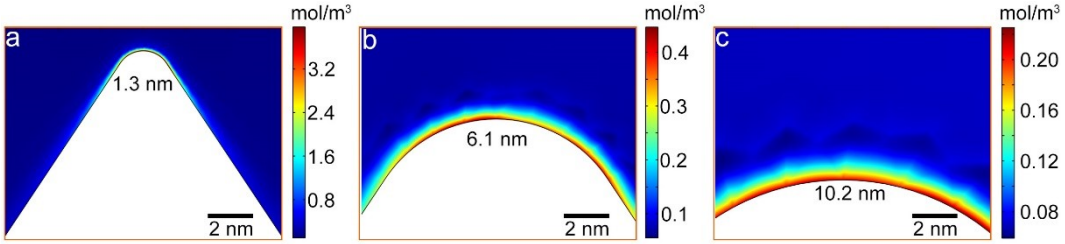

Figure S27. Surface K^+ density distributions on the surfaces of different tips.

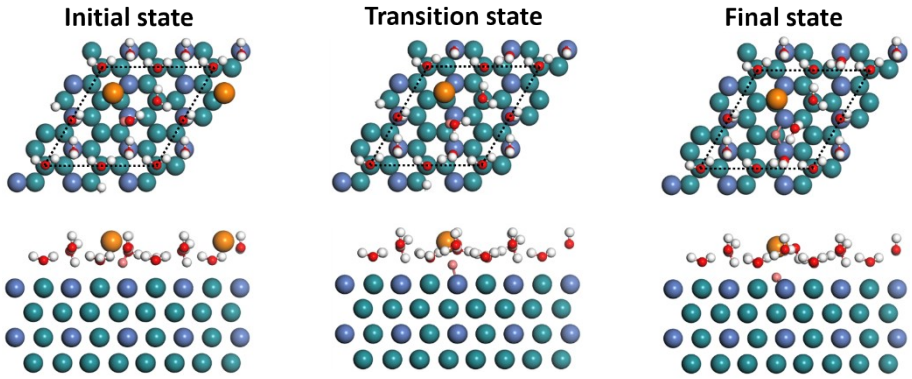

Figure S28. Atomic configurations of water dissociation step on the $Ru_3Ni(0001)$ surface with K^+. The orange, dark cyan, blue, red, and white spheres represent K, Ru, Ni, O, and H atoms, respectively. Pink sphere represents the dissociated H atom that adsorbs on the $Ru_3Ni(0001)$ surface.

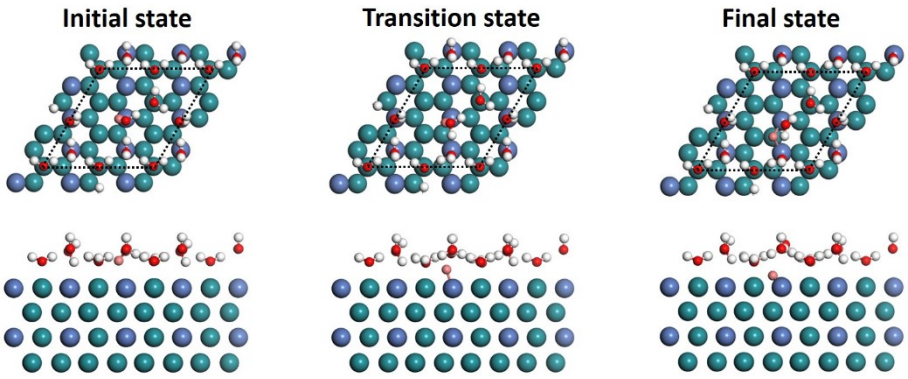

Figure S29. Atomic configurations of water dissociation step on the $Ru_3Ni(0001)$ surface without K^+. The dark cyan, blue, red, and white spheres represent Ru, Ni, O, and H atoms, respectively. Pink sphere represents the dissociated H atom that adsorbs on the $Ru_3Ni(0001)$ surface.

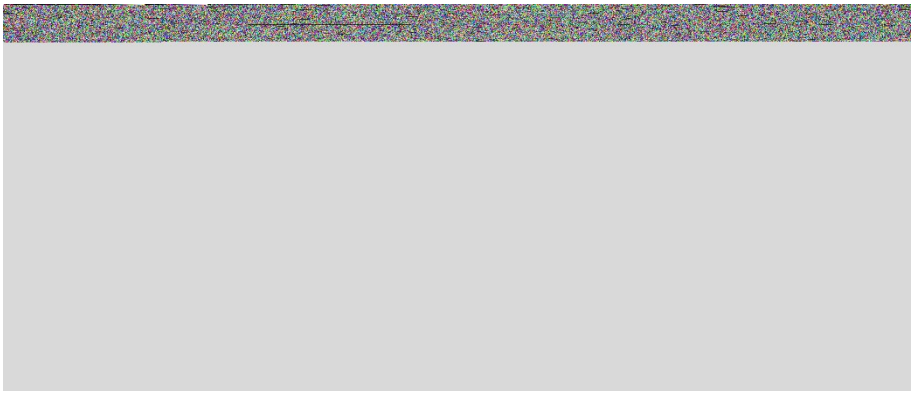

Figure S30. Atomic configurations of water dissociation step on $1e^-$ negatively charged $Ru_3Ni(0001)$ surface without K cation. The dark cyan, blue, red, and white spheres represent Ru, Ni, O, and H atoms, respectively. Pink sphere represents the dissociated H atom that adsorbs on the $Ru_3Ni(0001)$ surface.

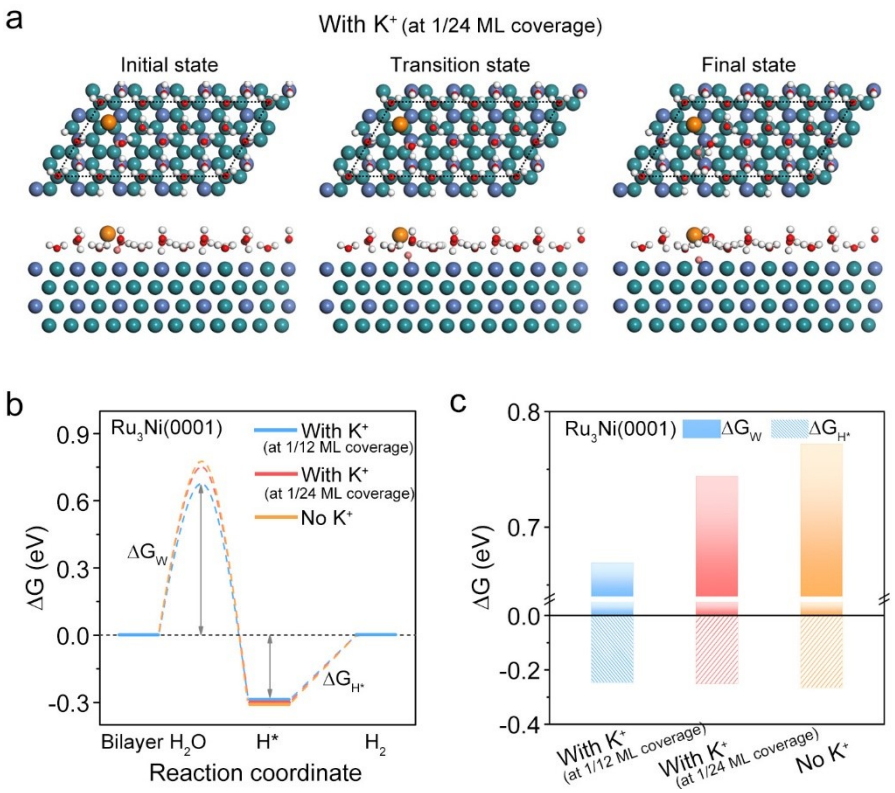

Figure S31. (a) Atomic configurations of water dissociation step on the $Ru_3Ni(0001)$ surface with K^+ at 1/24 ML coverage. The orange, dark cyan, blue, red, and white spheres represent K, Ru, Ni, O, and H atoms, respectively. Pink sphere represents the dissociated H atom that adsorbs on the $Ru_3Ni(0001)$ surface. (b) Gibbs free energy diagrams of alkaline HER on different systems including reactant initial state, intermediate state, final state, and an additional transition state representing water dissociation. ΔG_{H*} and ΔG_W represent hydrogen adsorption free energy and water dissociation free energy barrier, respectively. (c) The values of ΔG_{H*} and ΔG_W on different systems.

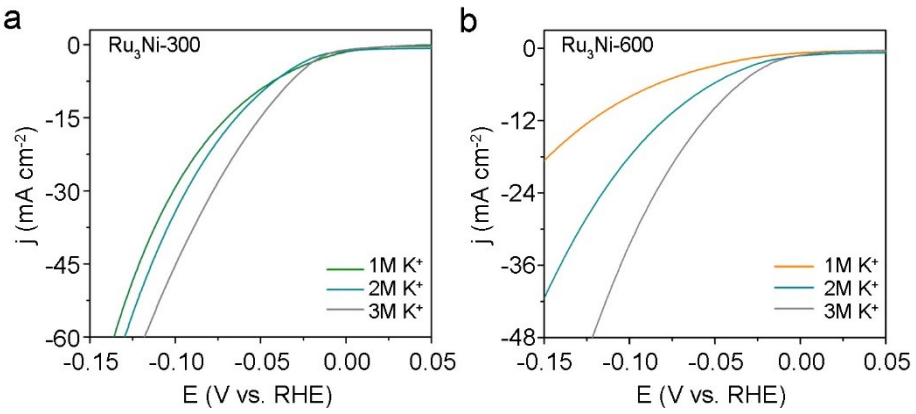

Figure S32. Polarization curves of (a) Ru_3Ni-300 and (b) Ru_3Ni-600 in electrolyte with different K^+ concentrations.

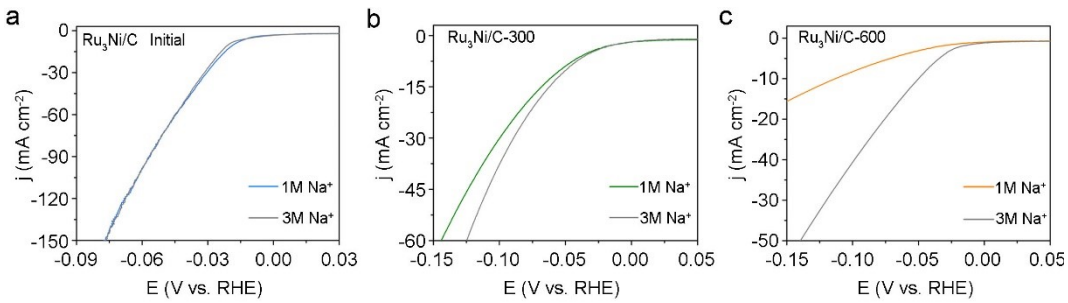

Figure S33. Polarization curves of (a) NA-Ru_3Ni, (b) Ru_3Ni-300, and (c) Ru_3Ni-600 in electrolyte with different Na^+ concentrations.

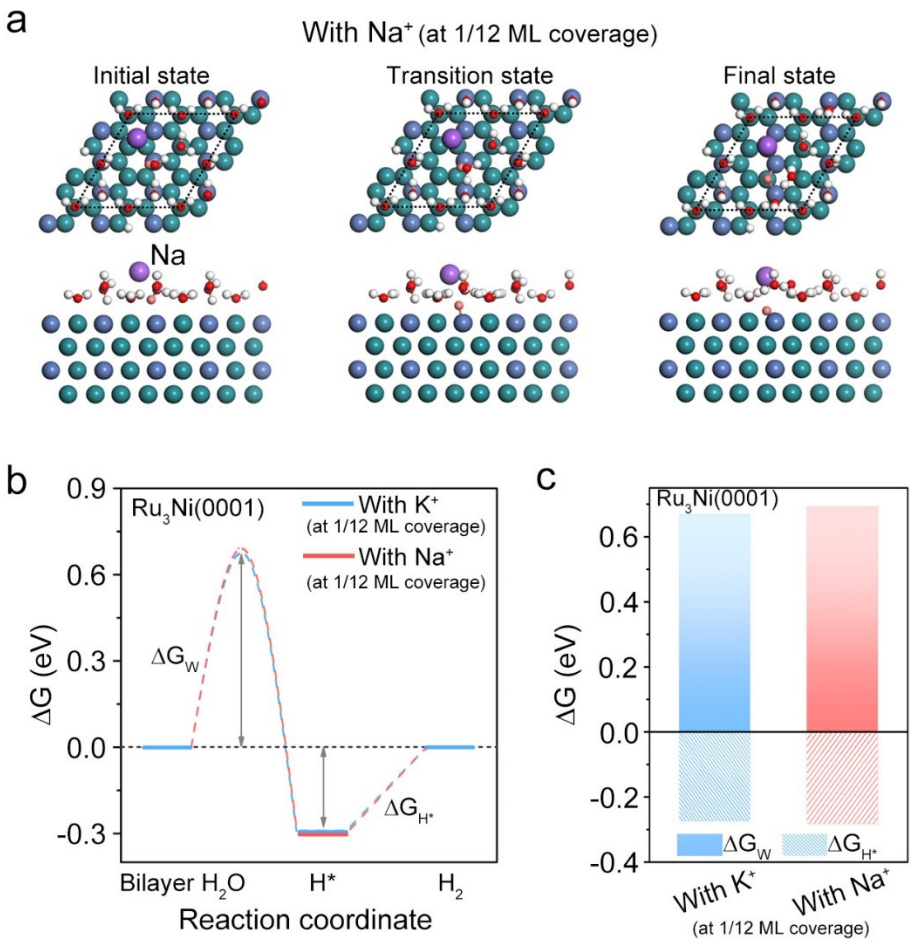

Figure S34. (a) Atomic configurations of water dissociation step on the $Ru_3Ni(0001)$ surface with Na^+ at 1/12 ML coverage. The purple, dark cyan, blue, red, and white spheres represent Na, Ru, Ni, O, and H atoms, respectively. Pink sphere represents the dissociated H atom that adsorbs on the $Ru_3Ni(0001)$ surface. (b) Gibbs free energy diagrams of alkaline HER on different systems including reactant initial state, intermediate state, final state, and an additional transition state representing water dissociation. ΔG_{H*} and ΔG_W represent hydrogen adsorption free energy and water dissociation free energy barrier, respectively. (c) The values of ΔG_{H*} and ΔG_W on different systems.

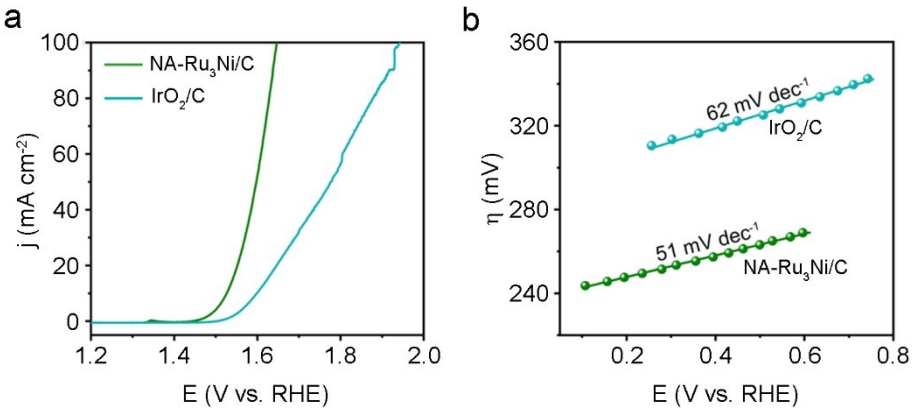

Figure S35. (a) OER polarization curves and (b) Tafel plots of NA-Ru_3Ni/C and commercial IrO_2/C catalysts.

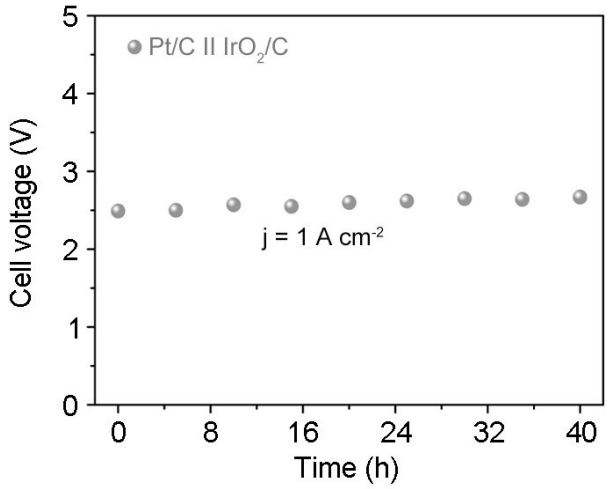

Figure S36. Chronopotentiometry curve for AEM electrolysis using Pt/C||IrO_2 couple operating at 1 A cm^{-2}.

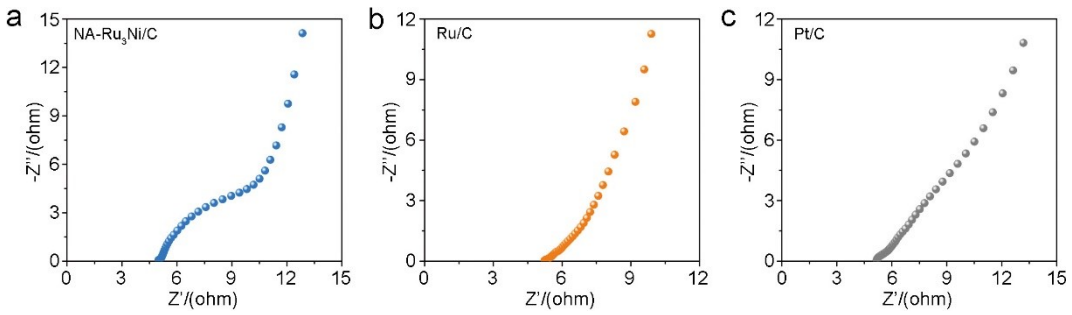

Figure S37. The Nyquist plots of (a) NA-Ru_3Ni/C, (b) Ru/C, and (c) Pt/C at open circuit voltage.

Table S1. Comparison of the HER activity for NA-Ru_3Ni electrocatalyst with reported Ru-based electrocatalysts in alkaline solution at current density of 10 mA cm^{-2}.

Catalysts	Electrode	Loading ($mg\ cm^{-2}$)	η_{10} (mV)	Tafel slop ($mV\ dec^{-1}$)	References
NA-Ru_3Ni	**RDE**	**0.08**	**14**	**28**	**This work**
2DPC-RuMo	GCE	0.25	18	25	13
RuCu NSs/250	GCE	--	20	15	14
RuCo@NC	GCE	0.28	28	31	15
NiFeRu-LDH	NF	--	29	31	16
Ru/np-MoS_2	Carbon cloth	--	30	31	17
Ru/Co_3O_4 NWs	CF	--	31	70	18
Ni@Ni_2P-Ru	GCE	0.29	31	35	19
Ru_1CoP/CDs-1000	RDE	0.42	51	73	20
Sr_2RuO_4	GCE	0.23	61	51	21
Ru_3Ni_3 NAs	GCE	0.10	39	26.9	22

Table S2. Comparison of the HER activity for NA-Ru_3Ni electrocatalyst with reported Ru-based electrocatalysts in alkaline solution at current density of 100 mA cm^{-2}.

Catalysts	Electrode	Loading (mg cm^{-2})	η_{100} (mV)	Reference
NA-Ru_3Ni	**RDE**	**0.08**	**53**	**This work**
Ru/MoO_2	RDE	0.25	90	23
RuP (L-RP)	GCE	0.46	93	24
RuCoP	GCE	0.30	102	25
Ru-NiCoP/NF	NF	--	103	26
Ru/Co_3O_4 NWs	CF	--	136	18
3D RuCu NCs	CP	1.33	147	27
RuNi/CQDs-600	GCE	0.42	193	28
$CoRu_{0.5}$/CQDs	GCE	0.46	215	29
Ru@CQDs480	GCE	0.42	228	30

Table S3 Comparison of the HER activity for NA-Ru_3Ni electrocatalyst with other reported electrocatalysts in 1 M KOH at current density of 1000 mA cm^{-2}.

Catalysts	Loading (mg cm^{-2})	η_{1000} (mV)	References
NA-Ru_3Ni	**0.08**	**168**	**This work**
Ru-Mo_2C@CNT	0.95	78	31
Ni_3S_2/Cr_2S_3@NF	1.25	261	32
Ru-CoO_x/NF	-	250	33
FeIr/NF	-	204	34
h-NiMoFe	0.5	98	35
$NiMoO_x$/NiMoS	-	236	36
A-NiCo LDH/NF	3.15	381	37
IrNi-$FeNi_3$/NF	-	289	38
Co-Mo_5N_6	4.3	280	39
Ni-P-B/Paper	5.63	345	40

Table S4. Comparison of Q_{CO} and ECSAs of as-synthesized NA-Ru_3Ni, the commercial Ru/C and Pt/C catalysts.

Catalysts	Q_{CO} (mC)	ECSA (m^2 g^{-1})
NA-Ru_3Ni	2.78	41.3
Commercial Ru/C	3.12	46.4
Commercial Pt/C	2.99	44.5

Table S5. Comparison of the TOF for NA-Ru_3Ni electrocatalyst with other reported electrocatalysts in alkaline solution at different overpotential.

Samples	Overpotential (mV)	TOF (H_2 s^{-1})	References
Ru_3Ni/C	**50**	**5.2**	**This Work**
Ru_3Ni/C	**100**	**26.5**	**This Work**
Ru@C_2N	25	0.8	41
$CoRu_{0.5}$/CQDs	60	6.4	28
Sr_2RuO_4	100	0.9	21
Ru@MWCNT	25	0.4	42
Ru-Mo_2C@CNT	100	21.9	31
2DPC-RuMo	50	3.6	13
RuNi NSs	50	1.6	43
Ru SAs–Ni_2P	57	1.0	44
Ni@Ni_2P-Ru	100	1.1	19
R-NiRu	100	0.78	45
Ru@NC(-0.2)	100	10.8	46
WS_2 MSLs	200	0.74	47

Table S6. Comparison of the stability for NA-Ru_3Ni electrocatalyst with other reported electrocatalysts in alkaline solution at different current density.

Samples	Current density ($mA\ cm^{-2}$)	Time (h)	References
NA-Ru_3Ni	**100**	**1450**	**This work**
Ru@Ni-MOF	10	24	48
RuO_2-300Ar	50	0.5	49
Ru@NC(-0.2)	35	12	46
Ru_1/D-NiFe LDH	100	50	50
RuNi NSs	83	10	43
$CoRu_{0.5}$/CQDs	20	100	28
Ru_2P/WO_3@NPC	10	21	51
2DPC-RuMo	10	120	13
Ru/np-MoS_2	10	40	17

Table S7. Comparison of Q_{CO}, ECSAs, the number of active sites and TOF values (at the overpotential of 50 mV) of our synthesized NA-Ru_3Ni, the commercial Ru/C and Pt/C catalysts.

Samples	Q_{CO} (mC)	ECSA (m^2 g^{-1})
NA-Ru_3Ni (After dealloying)	3.06	45.6
Ru_3Ni-300	2.20	32.8
Ru_3Ni-300 (After dealloying)	2.35	35.0
Ru_3Ni-600	1.02	15.2
Ru_3Ni-600 (After dealloying)	1.38	20.6

Table S8. The charge distribution of each slab and electrolyte interface for $Ru_3Ni(0001)$ based on Bader analysis.

Models	Slab surface (e^-)	Electrolyte (e^-)
With K^+	0.94	-0.94
No K^+, N = -1	1.04	-0.04
No K^+	0.17	-0.17

Table S9 Comparison of the AEM activity for NA-Ru_3Ni electrocatalyst with other reported electrocatalysts.

Catalysts	Cell voltage (V @ mA cm^{-2})	Stability (h)	Degradation of voltage (%)	Ref.
NA-Ru_3Ni/C||NA-Ru_3Ni/C	**2.05@1.0**	**2000**	**5.3**	**This work**
Pt/C||IrO_2/C	2.49@1.0	40	7.2	This work
Ni_3S_2/Cr_2S_3@NF||NiFeCr-LDH@NF	2.04@1.0	35	6.9	32
FeP–CoP/NC||FeP–CoP/NC	2.10@0.75	24	1.8	52
LSC/K-$MoSe_2$||LSC/K-$MoSe_2$	2.52@1.0	800	-	53
VCoP-2/Ni||VCoP-2/Ni	2.10@1.0	100	5.0	54
LSC&$MoSe_2$||LSC&$MoSe_2$	2.30@1.0	1000	10.9	55

References

(1) Gilliam, R. J. et al. A review of specific conductivities of potassium hydroxide solutions for various concentrations and temperatures. *Int. J. Hydrog. Energy* **32**, 359–364 (2007).

(2) Friedman, A. M. & Kennedy, J. W. The self-diffusion coefficients of potassium, cesium, iodide and chloride ions in aqueous solutions. *J. Am. Chem. Soc*. **77**, 4499–4501 (1955).

(3) Kallikragas, D. T. et al. High temperature diffusion coefficients for O_2, H_2, and OH in water, and for pure water. *J. Chem. Eng. Data* **59**, 1964–1969 (2014).

(4) Kresse, G. & Hafner, J. Ab initio molecular–dynamics simulation of the liquid–metal–amorphous–semiconductor transition in germanium. *Phys. Rev. B* **49**, 14251–14269 (1994).

(5) Kresse, G. & Joubert, D. From ultrasoft pseudopotentials to the projector augmented–wave method. *Phys. Rev. B* **59**, 1758–1775 (1999).

(6) Kresse, G. & Furthmüller, J. Efficient iterative schemes for Ab initio total-energy calculations using a plane-wave basis set. *Phys. Rev. B* **54**, 11169–11186 (1996).

(7) Perdew, J. P. et al. Generalized gradient approximation made simple. *Phys. Rev. Lett*. **77**, 3865–3868 (1996).

(8) Grimme, S. et al. A consistent and accurate Ab initio parametrization of density functional dispersion correction (DFT-D) for the 94 elements H-Pu. *J. Chem. Phys*. **132**, 154104 (2010).

(9) Monkhorst, H. J. & Pack, J. D. Special points for Brillouin–zone integrations. *Phys. Rev. B* **13**, 5188–5192 (1976).

(10) Henkelman, G. et al. A climbing image nudged elastic band method for finding saddle points and minimum energy paths. *J. Chem. Phys*. **113**, 9901–9904 (2000).

(11) Wang, P. et al. Precise tuning in platinum-nickel/nickel sulfide interface nanowires for synergistic hydrogen evolution catalysis. *Nat. Commun*. **8**, 14580 (2017).

(12) Nørskov, J. K. et al. Trends in the exchange current for hydrogen evolution. *J. Electrochem. Soc*. **152**, J23–J26 (2005).

(13) Tu, K. et al. A novel heterostructure based on RuMo nanoalloys and N-doped carbon as an efficient electrocatalyst for the hydrogen evolution reaction. *Adv. Mater*. **32,** 2005433 (2020).

(14) Yao, Q. et al. Channel-rich RuCu nanosheets for pH-universal overall water splitting electrocatalysis. *Angew. Chem. Int. Ed*. **58**, 13983–139883 (2019).

(15) Su, J. et al. Ruthenium-cobalt nanoalloys encapsulated in nitrogen-doped graphene as active electrocatalysts for producing hydrogen in alkaline media. *Nat. Commun*. **8**, 14969 (2017).

(16) Chen, G. et al. Accelerated hydrogen evolution kinetics on NiFe-layered double hydroxide electrocatalysts by tailoring water dissociation active sites. *Adv. Mater*. **30,** 1706279 (2018).

(17) Jiang, K. et al. Rational strain engineering of single-atom ruthenium on nanoporous MoS_2 for highly efficient hydrogen evolution. *Nat. Commun*. **12**, 1687 (2021).

(18) Liu, Z. et al. Charge redistribution of Ru nanoclusters on Co_3O_4 porous nanowire via the oxygen regulation for enhanced hydrogen evolution reaction. *Nano Energy* **85**, 105940 (2021).

(19) Liu, Y. et al. Ru modulation effects in the synthesis of unique rod-like Ni@Ni_2P–Ru heterostructures and their remarkable electrocatalytic hydrogen evolution performance. *J. Am. Chem. Soc*. **140**, 2731–2734 (2018).

(20) Song, H. et al. Single atom ruthenium-doped CoP/CDs nanosheets via splicing of carbon-dots for robust hydrogen production. *Angew. Chem. Int. Ed*. **60**, 7234–7244 (2021).

(21) Zhu, Y. et al. Unusual synergistic effect in layered Ruddlesden−Popper oxide enables ultrafast hydrogen evolution. *Nat. Commun*. **10**, 149 (2019).

(22) Yang, J. et al. pH-universal water splitting catalyst: Ru-Ni nanosheet assemblies. *iScience* **11**, 492–504 (2019).

(23) Li, H. et al. Paired Ru–O–Mo ensemble for efficient and stable alkaline hydrogen evolution reaction. *Nano Energy* **82**, 105767 (2021).

(24) Yu, J. et al. Bigger is surprisingly better: agglomerates of larger RuP nanoparticles outperform benchmark Pt nanocatalysts for the hydrogen evolution reaction. *Adv. Mater*. **30,** 1800047 (2018).

(25) Xu, J. et al. Boosting the hydrogen evolution performance of ruthenium clusters through synergistic coupling with cobalt phosphide. *Energy Environ. Sci*. **11**, 1819–1827 (2018).

(26) Chen, D. et al. Ru-doped 3D flower-like bimetallic phosphide with a climbing effect on overall water splitting. *Appl. Catal. B: Environ*. **279**, 119396 (2020).

(27) Cao, D. et al. Growth of highly active amorphous RuCu nanosheets on Cu nanotubes for the hydrogen evolution reaction in wide pH values. *Small* **16**, 2000924 (2020).

(28) Liu, Y. et al. A general route to prepare low-ruthenium-content bimetallic electrocatalysts for pH-universal hydrogen evolution reaction by using carbon quantum dots. *Angew. Chem. Int. Ed*. **59**, 1718–1726 (2020).

(29) Li, W. et al. Exploiting Ru-induced lattice strain in CoRu nanoalloys for robust bifunctional hydrogen production. *Angew. Chem. Int. Ed*. **60**, 3290–3298 (2021).

(30) Li, W. et al. Carbon-quantum-dots-loaded ruthenium nanoparticles as an efficient electrocatalyst for hydrogen production in alkaline media. *Adv. Mater*. **30**, 1800676 (2018).

(31) Wu, X. et al. Solvent-free microwave synthesis of ultra-small Ru-Mo_2C@CNT with strong metal-support interaction for industrial hydrogen evolution. *Nat. Commun*. **12**, 4018 (2021).

(32) Fu, H. Q. et al. Hydrogen spillover-bridged Volmer/Tafel processes enabling ampere-level current density alkaline hydrogen evolution reaction under low overpotential. *J. Am. Chem. Soc*. **144**, 6028–639 (2022).

(33) Wu, D. et al. Ultralow Ru incorporated amorphous cobalt-based oxides for high-current-density overall water splitting in alkaline and seawater media. *Small* **17**, 2102777 (2021).

(34) Shen, F. et al. Bimetallic iron-iridium alloy nanoparticles supported on nickel foam as highly efficient and stable catalyst for overall water splitting at large current density. *Appl. Catal. B: Environ*. **278**, 119327 (2020).

(35) Luo, Y. et al. Stabilized hydroxide-mediated nickel-based electrocatalysts for high-current-density hydrogen evolution in alkaline media. *Energy Environ. Sci*. **8**, 4610–4619 (2021).

(36) Zhai, P. et al. Engineering active sites on hierarchical transition bimetal oxides/sulfides heterostructure array enabling robust overall water splitting. *Nat. Commun*. **11**, 5462 (2020).

(37) Yang, H. et al. B-doping-induced amorphization of LDH for large-current-density hydrogen evolution reaction. *Appl. Catal. B: Environ*. **261**, 118240 (2020).

(38) Wang, Y. et al. Industrially promising IrNi-$FeNi_3$ hybrid nanosheets for overall water splitting catalysis at large current density. *Appl. Catal. B: Environ*. **286**, 119881 (2021).

(39) Lin, F. et al. Electrocatalytic hydrogen evolution of ultrathin Co-Mo_5N_6 heterojunction with interfacial electron redistribution. *Adv. Energy Mater*. **10**, 2002176 (2020).

(40) Hao, W. et al. Fabrication of practical catalytic electrodes using insulating and eco-friendly substrates for overall water splitting. *Energy Environ. Sci*. **13**, 102–110 (2020).

(41) Mahmood, J. et a. An efficient and pH-universal ruthenium-based catalyst for the hydrogen evolution reaction. *Nat. Nano.* **12**, 441–446 (2017).

(42) Kweon, D. et al. Ruthenium anchored on carbon nanotube electrocatalyst for hydrogen production with enhanced Faradaic efficiency. *Nat. Commun*. **11**, 1278 (2020).

(43) Liu, G. Synthesis of RuNi alloy nanostructures composed of multilayered nanosheets for highly efficient electrocatalytic hydrogen evolution. *Nano Energy* **66**, 104173 (2019).

(44) Wu, K. et al. Atomically dispersed Ni–Ru–P interface sites for high-efficiency pH-universal electrocatalysis of hydrogen evolution. *Nano Energy* **80**, 105467 (2021).

(45) Chen, X. et al. Atomically dispersed ruthenium on nickel hydroxide ultrathin nanoribbons for highly efficient hydrogen evolution reaction in alkaline media. *Adv. Mater*. **33**, 2104764 (2021).

(46) Wang, Z.-L. et al. Spatially confined assembly of monodisperse ruthenium nanoclusters in a hierarchically ordered carbon electrode for efficient hydrogen evolution. *Angew. Chem. Int. Ed*. **130**, 5950–5954 (2018).

(47) Xie, L. WS_2 moiré superlattices derived from mechanical flexibility for hydrogen evolution reaction. *Nat. Commun*. **12**, 5070 (2021).

(48) Deng, L. et al. Electronic modulation caused by interfacial Ni-O-M (M=Ru, Ir, Pd) bonding for accelerating hydrogen evolution kinetics. *Angew. Chem. Int. Ed*. **60**, 22276–22282 (2021).

(49) Dang, Y. et al. Partially reduced Ru/RuO_2 composites as efficient and pH-universal electrocatalysts for hydrogen evolution. *Energy Environ. Sci*. **14**, 5433–5443 (2021).

(50) Zhai, P. et al. Engineering single-atomic ruthenium catalytic sites on defective nickel-iron layered double hydroxide for overall water splitting. *Nat. Commun*. **12**, 4587 (2021).

(51) Jiang, X. et al. The heterostructure of Ru_2P/WO_3/NPC synergistically promotes H_2O dissociation for improved hydrogen evolution. *Angew. Chem. Int. Ed*. **133**, 4156–4162 (2021).

(52) Yan, X. et al. A membrane-free flow electrolyzer operating at high current density using earth-abundant catalysts for water splitting. *Nat. Commun.* **12**, 4143 (2021).

(53) Oh, N. K. et al. Highly efficient and robust noble-metal free bifunctional water electrolysis catalyst achieved via complementary charge transfer. *Nat. Commun.* **12**, 4606 (2021).

(54) Wan, L. et al. Overall design of novel 3D-ordered MEA with drastically enhanced mass transport for alkaline electrolyzers. *Energy Environ. Sci.* **15**, 1882 (2022).

(55) Oh, N. K. et al. In-situ local phase-transitioned $MoSe_2$ in $La_{0.5}Sr_{0.5}CoO_{3-\delta}$ heterostructure and stable overall water electrolysis over 1000 hours. *Nat. Commun.* **10**, 1723 (2019).